# Using a microscopic mechanical resonator in a millikelvin environment to probe the CSL model

Jong, Thijmen de

# Using a microscopic mechanical resonator in a millikelvin environment to probe the CSL model

THESIS

submitted in partial fulfillment of the
requirements for the degree of

MASTER OF SCIENCE
in
PHYSICS


| | |
|---|---|
| Author : | T.C. de Jong BSc |
| Student ID : | s2488477 |
| Supervisor : | Prof. Dr. Ir. T.H. Oosterkamp |
| | Ir. L.R. van Everdingen |
| Second corrector : | Dr. W. Löffler |


Leiden, The Netherlands, August 8, 2025

# Using a microscopic mechanical resonator in a millikelvin environment to probe the CSL model

**T.C. de Jong BSc**

Huygens-Kamerlingh Onnes Laboratory, Leiden University
P.O. Box 9500, 2300 RA Leiden, The Netherlands

August 8, 2025

## Abstract

One of the important questions in modern quantum mechanics is the mechanism behind wavefunction collapse. One possible answer to this problem is formulated in the continuous spontaneous localization model. This model states that quantum systems collapse spontaneously. This spontaneous collapse generates a small amount of energy. We attempt to measure this using a mechanical oscillator which is supercooled in a dry dilution refrigerator with a nuclear demagnetization stage. In this thesis we discuss the results of a measurement run where we reach a cryostat temperature of 3 mk and cantilever Q-factor of approximately $1.4{\cdot}10^3$. Furthermore we test a newly designed detection chip which shows promising results for use in the setup for the CSL experiment. The results of the measurement run do not further constrain the upper bounds of the CSL parameters, but do give us a lot of information on how to improve the setup for future measurements.

# Contents





Version of August 8, 2025– Created August 8, 2025 - 13:34

Chapter 1

# Introduction

Since the inception of quantum mechanics in the twentieth century, our knowledge of the quantum world has greatly increased. Naturally, new questions and problems have arisen. The main problem quantum physicists are trying to solve is how to join the two fundamental physical theories: quantum mechanics and general relativity. A different but equally important question which still needs answering is the so-called measurement problem. This measurement problem originates from the superposition principle. Quantum mechanics tells us that for a quantum system with states $|0\rangle$ and $|1\rangle$, the linear combination of these states $\alpha|0\rangle + \beta|1\rangle$ is also a possible state. In other words, a quantum system (or particle) can be in two states (or places) at once. However, the idea that a macroscopic system can be in multiple states at once seems impossible. You cannot measure a particle in two places at once, Schrödingers cat cannot be simultaneously alive and dead.[1]. Many theories regarding the measurement problem have been proposed. A large step towards verifying these theories would be to place a macroscopic object in a quantum superposition.

## 1.1 Motivation

The theories which attempt to solve the measurement problem can all be categorized in broader interpretations. One of these interpretations is called the many worlds interpretation (MWI). The MWI is based on the postulate that all isolated systems evolve according to the Schrödingers equation $\frac{d}{dt}|\psi\rangle = -\frac{i}{\hbar}H|\psi\rangle$. This means that the above described state of $\alpha|0\rangle + \beta|1\rangle$ actually does not collapse into either $|0\rangle$ or $|1\rangle$ when measured with the probability of $|\alpha^2|$ and $|\beta^2|$ respectivelyWe cannot see this

superposition because our view is subjective, our view is from an observer inside the system. The macrosuperpositions are rapidly destroyed due to environment-induced superpositions according to our view, but the objective mathematical view of the world remains intact, including the evolving wavefunction.[2] The main problem with the MWI is that it is impossible to verify experimentally.

A counterpart to the MWI is the Copenhagen interpretation. This interpretation states that there is a distinct separation between the quantum world and the classical world. The quantum mechanical wavefunction collapses and vanishes when a quantum system is measured as opposed to the MWI. The only thing that remains is the outcome of the measurement, either $|0\rangle$ or $|1\rangle$. This means that the outcome of any quantum measurement is entirely non deterministic. The outcome of a measurement is based on probabilities calculated with the wave function.[3]

With this interpretation new problems arise. Questions like "what defines a measurement?" And why should the state of a system be dependent on the actions of outside observers? Similar to the Copenhagen interpretation, objective-collapse theories, or dynamical reduction models, assume the total collapse of the wavefunction. However, this collapse is not dependent on the actions of observers. The main principle of these theories is that the collapse of the wavefunction is the consequence of the basic laws of nature. This is achieved by adding a stochastic term to the Schrödingers equation, which describes the state reduction occurring in the system. This means that the theory proposed in [4], Ghirardi Rimini Weber theory (GRW) is not strictly an interpretation of quantum mechanics, but a new quantum theory. In GWR theory it is stated that quantum states collapse spontaneously. On average $10^{-16}$ of these so-called hits or spontaneous localizations occur every second. Therein lies the solution to the measurement problem. For a macroscopic system that is made up of around $10^{23}$ atoms, there are $10^{7}$ hits every second and superpositions are suppressed almost immediately. Quantum systems are hit very rarely and retain their superposition for a long time.[5]

GWR theory is not perfect. A different theory based on GWR theory solved the problems which appeared in GWR theory. It is similar to GWR theory as it is based on spontaneous collapse of the wavefunction. The large difference, however, is that the discontinuous hits are replaced by a continuous stochastic evolution of the states, hence the name continuous spontaneous localization theory (CSL).[6] An additional advantage of

the spontaneous collapse models is that they are experimentally testable. CSL theory postulates that the collapsing of the wave function causes noise. This noise manifests itself as thermal energy generation, in other words, the collapsing of a wavefunction heats up the system. This small increase in temperature can theoretically be measured and with it prove CSL theory.[7]

## 1.2 Goal

As stated earlier, the proposed excess energy released by the collapsing wavefunction is very small. Therefore, the thermal noise created by the collapsing wavefunction is indistinguishable from other noise sources such as resonances in the system. Therefore experiments concerning CSL generally give upper bounds for the relevant CSL parameters. By minimizing other noise sources a noise floor will appear which will then set the upper bound for the CSL parameters.

To do this, we use a non-interferometric approach. We use an MRFM (Magnetic resonance force microscopy) setup in a dry dilution refrigerator. MRFM is a method for measuring individual electron spins in a sample. Since we will not be using the setup for this purpose, we will not dive into the details of MRFM. The magnetic cantilever in the setup, however, is used for as a low temperature force sensor. The refrigerator will cool the setup to $\sim$20 mk and a nuclear demagnetization stage (NDS) cools it to sub 10 mk temperatures. The movement of the cantilever is measured using a SQUID (superconducting quantum interference device). We will test a new version of the detection chip used which will ideally improve the coupling between the cantilever and the SQUID chip by an order of magnitude. This will ultimately mean we will achieve a better signal to noise ratio and lower the noise floor of our measurements.

Chapter 2

# Theory

## 2.1 The CSL model

Let us first dive deeper into CSL theory. This section is based on the review by Bassi et al.[8]

### 2.1.1 Objective-collapse theories

As stated in the introduction, CSL is a theory which attempts to solve the measurement problem and falls under the objective-collapse theories. These theories modify the Schrödinger equation

$$i\hbar\frac{\partial}{\partial t}\Psi(x,t) = \left[-\frac{\hbar^2}{2m}\frac{\partial^2}{\partial x^2} + V(x,t)\right]\Psi(x,t) = H\Psi(x,t) \tag{2.1}$$

by adding terms. These new terms should have the following properties:

- The new terms must be nonlinear. Any quantum mechanical superposition must break at the macroscopic level and the wavefunction must be localized.
- The new terms must be stochastic. The outcomes of measurements are non deterministic so these new terms must explain why they are random.
- There must be some kind of amplification mechanism. For quantum systems, the effect of the new terms should be negligible but for large systems their effect should be very strong. In other words, quantum systems retain their superposition, while macroscopic systems behave classically.

- They must not allow for faster-than-light communication.

These conditions are not easily met. One of the greatest achievements of modern collapse models is successfully and consistently implementing the above described conditions.

### 2.1.2 Parameters

There are two important parameters in CSL theory, namely $r_c$ and $\lambda$. To show where these parameters come from and what their physical meaning is, let us briefly review GRW theory.

We look at an arbritrary state described by a wave function $\psi(\mathbf{x}_1, \mathbf{x}_2, \ldots, \mathbf{x}_N)$. According to GRW theory, this state will experience a jump at random times of the form

$$\psi_t(\mathbf{x}_1, \mathbf{x}_2, \ldots, \mathbf{x}_N) \rightarrow \frac{L_n(\mathbf{x})\psi_t(\mathbf{x}_1, \mathbf{x}_2, \ldots, \mathbf{x}_N)}{||L_n(\mathbf{x})\psi_t(\mathbf{x}_1, \mathbf{x}_2, \ldots, \mathbf{x}_N)||} \tag{2.2}$$

$\psi_t(\mathbf{x}_1, \mathbf{x}_2, \ldots, \mathbf{x}_N)$ represents the state vector at time $t$, just before the jump occurs. $L_n(\mathbf{x})$ is a linear operator given by

$$L_n(\mathbf{x}) = \frac{1}{(\pi r_c^2)^{\frac{3}{4}}} e^{(\mathbf{q}_n - \mathbf{x})^2 / 2r_c^2} \tag{2.3}$$

Here we encounter the first of two parameters. $r_c$ is the correlation length and sets the width of the localization process. $\mathbf{q}_n$ is the position of the $n$th particle and $\mathbf{x}$ corresponds to the place where the jump occurs. The probability density for a jump taking place at position $\mathbf{x}$ for the $n$th particle is given by

$$p_n(\mathbf{x}) \equiv ||L_n(\mathbf{x})\psi_t(\mathbf{x}_1, \mathbf{x}_2, \ldots, \mathbf{x}_N)||^2 \tag{2.4}$$

It is assumed that these jumps are distributed in time according to a Poissonanian process. The frequency of this random process is given by the second parameter $\lambda$, the collapse rate. Both parameters appear in the following equation which describes the superposition collapse of a single particle:

$$\langle \mathbf{x}| \, T[\rho(t)] \, |\mathbf{y}\rangle = \lambda_{GWR} \left[ 1 - e^{\frac{-(\mathbf{x}-\mathbf{y})^2}{4r_c^2}} \right] \langle \mathbf{x}| \, \rho(t) \, |\mathbf{y}\rangle \tag{2.5}$$

$\rho(t)$ is the density matrix $|\psi_t\rangle \langle\psi_t|$. As expected the effect of spontaneous collapse suppresses the off-diagonal components. $T$ represents the effect on the wavefunction of the spontaneous collapses.



Version of August 8, 2025– Created August 8, 2025 - 13:34

For the GRW model the numerical values of the two described parameters are $\lambda_{\text{GRW}} \simeq 10^{-16}\text{s}^{-1}$ and $r_c \simeq 10^{-7}\text{m}$.[9] With these numerical values three important properties have been proven. First: at the microscopic level, quantum systems behave as predicted by "standard" quantum mechanics. Second: At the macroscopic level wave functions of massive objects are always well localized in space and their center of mass move according to Newton's laws of motion. Lastly, the outcomes of measurements on quantum systems follow the Born probability rule according to the GRW model.

### 2.1.3 CSL

The most advanced spontaneous collapse model as of today is the Continuous spontaneous localization model. It is defined by the following stochastical differential equation:

$$d\psi_t = [-\frac{i}{\hbar}Hdt + \frac{\sqrt{\gamma}}{m_0}\int d\mathbf{x}[M(\mathbf{x}) - \langle M(\mathbf{x})\rangle_t]dW_t(\mathbf{x}) - \frac{\gamma}{2m_0^2}\int d\mathbf{x}[M(\mathbf{x}) - \langle M(\mathbf{x})\rangle_t]^2 dt]\psi_t \tag{2.6}$$

$H$ is the standard Hamiltonian. The two other terms are the added terms which follow the prerequisites laid out in section 2.1.1 and induce the collapse of the wave function. $m_0$ is a reference mass usually taken as the mass of a nucleon. $\gamma$ is a positive coupling constant which determines the strength of the collapse. $M(\mathbf{x})$ is a smeared mass density operator:

$$M(\mathbf{x}) = \sum_j m_j N_j(\mathbf{x}) \tag{2.7}$$

$$N_j(\mathbf{x}) = \int d\mathbf{y} g(\mathbf{y} - \mathbf{x})\psi_j^\dagger(\mathbf{y})\psi_j(\mathbf{y}) \tag{2.8}$$

$\psi_j^\dagger(\mathbf{y})$ and $\psi_j(\mathbf{y})$ are the creation and annihilation operator of particle $j$ at a point in space $\mathbf{y}$. The function $g(\mathbf{x})$ gives a distribution of the mass:

$$g(\mathbf{x}) = \frac{1}{(\sqrt{2\pi}r_c)^3}e^{\frac{-\mathbf{x}^2}{2r_c^2}} \tag{2.9}$$

The first of the two parameters introduced in section 2.1.2 appears in this function. The correlation length $r_c$ determines how much the mass is

"smeared out" out over space. Lastly $W_t(\mathbf{x})$ is an ensemble of independent Wiener processes. A Wiener process is a continuous time stochastic process comparable with Brownian motion[10]. This ensemble contains a stochastic process for every point in space. The density number operators $\psi_j^\dagger(\mathbf{y})\psi_j(\mathbf{y})$ in equation 2.8 are responsible for the collapse of the wavefunction. They suppress superpositions containing different numbers of particles in different points of space.

To look at the collapse itself, we again consider the suppression of the off diagonal components of the density matrix. The time induced decay of a many-nucleon system (we ignore the decay of electrons) is

$$\frac{\partial}{\partial t}\left\langle \bar{\mathbf{x}}' \right| \rho_t \left| \bar{\mathbf{x}}'' \right\rangle = \Gamma(\bar{\mathbf{x}}', \bar{\mathbf{x}}'') \left\langle \bar{\mathbf{x}}' \right| \rho_t \left| \bar{\mathbf{x}}'' \right\rangle \tag{2.10}$$

$$\Gamma = \frac{\gamma}{2}\sum_{i,j}\left[G(\bar{\mathbf{x}}_i' - \bar{\mathbf{x}}_j') + G(\bar{\mathbf{x}}_i'' - \bar{\mathbf{x}}_j'') - 2G(\bar{\mathbf{x}}_i' - \bar{\mathbf{x}}_j'')\right] \tag{2.11}$$

Where $\bar{\mathbf{x}}' \equiv \bar{\mathbf{x}}_1, \bar{\mathbf{x}}_2, \ldots, \bar{\mathbf{x}}_N$ and similar for $\bar{\mathbf{x}}''$. $\Gamma$ is the decay function.

$$G(\mathbf{x}) = \frac{1}{(4\pi r_c^2)^{\frac{3}{2}}} e^{\frac{-\mathbf{x}^2}{4r_c^2}} \tag{2.12}$$

If we consider a system with only one nucleon, equation 2.11 reduces to

$$\Gamma(\mathbf{x}', \mathbf{x}'') = \frac{\gamma}{(4\pi r_c^2)^{\frac{3}{2}}}\left[1 - e^{\frac{-|\mathbf{x}'-\mathbf{x}''|^2}{4r_c^2}}\right] \tag{2.13}$$

This is exactly equation 2.5 with $\lambda_{CSL}$ instead of $\lambda_{GWR}$

$$\lambda_{CSL} = \frac{\gamma}{(4\pi r_c^2)^{\frac{3}{2}}} \tag{2.14}$$

The first estimate for $\gamma$ was $\gamma \sim 10^{-30}$ cm$^3$s$^{-1}$, which corresponds to $\lambda_{\text{CSL}} \sim 2.2 \times 10^{-17}$ s$^{-1}$. However, experiments have narrowed down the possible values for $\lambda$ and $r_c$. The shaded regions in figure 2.1 shows the values ruled out. Only the white region still needs experimental verification.

Let us define $l = ||\mathbf{x}' - \mathbf{x}''||$ where $l$ is the distance between two particles in superposition. We can now deduce from equations 2.11 and 2.12, that the contribution to the wave function collapse for a particle in superposition

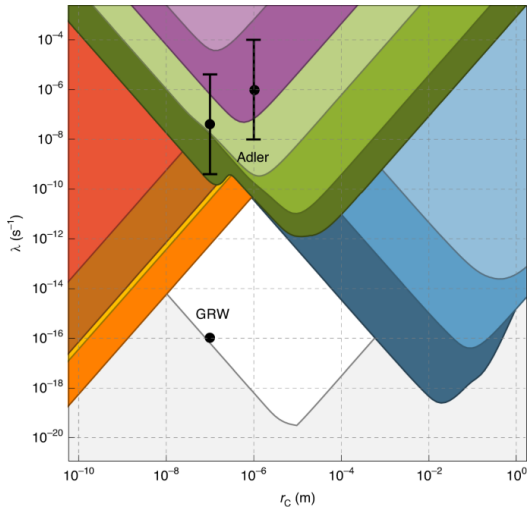


***Figure 2.1:*** *Graph showing the possible values for $\lambda$ and $r_c$. The shaded regions are ruled out by experimental tests. It is important to note that this graph is mostly illustrative and outdated as lower bounds have already been set.[11] The green regions are from cantilever-based experiments and multilayer structures. The blue areas are obtained from gravitational wave detectors. The purple areas are from levitating optomechanical systems. The orange, red and brown regions are obtained from various heating and excitation experiments. Obtained from Carlesso et al. [12]*

with $l \ll r_C$ is negligible. However, when $l$ starts to approach $r_c$, $G$ starts to increase quadratically. Furthermore, for $l > r_c$ $\Gamma$ increases linearly. This leads to the simplified formula

$$\Gamma = \lambda_{CSL} n^2 N \tag{2.15}$$

where $n$ is the number of particles with $l < r_C$ and $N$ is the total number of those clusters. This implies the expected result that the larger the system, the higher the decay rate.

Now that we have a basic framework of the CSL model and how it governs superposition collapse, let us look at the implications of the model regarding the force noise on a cantilever setup. We consider the Hamiltonian of a standard quantum mechanical harmonic oscillator with an added stochastic potential which mimics the effect of the CSL model.

$$\hat{H} = \frac{1}{2m}\hat{p} + \frac{1}{2}m\omega_0\hat{q}^2 - \hbar w_t \sqrt{\eta}\hat{q} \tag{2.16}$$

where $\hat{p}$ and $\hat{q}$ are the standard momentum and position operators. $w_t$ is a white noise, with zero average and delta correlation function. $\eta$ is defined by the following formula

$$\eta = \frac{(4\pi)^{\frac{3}{2}}\lambda r_c^3}{m_0^2}\int \frac{d^3\mathbf{k}}{(2\pi)^3} k_z^2 e^{-\mathbf{k}^2 r_c^2}|\tilde{\rho}(\mathbf{k})|^2 \tag{2.17}$$

with $\mathbf{k} = (k_x, k_y, k_z)$, $\tilde{\rho}(\mathbf{k}) = \int d^3\mathbf{x} e^{i\mathbf{k}\cdot\mathbf{r}}\rho(\mathbf{r})$. $\rho(\mathbf{r})$ is the mass density of the oscillator. Combining these expressions gives the equilibrium energy of the system $\langle\hat{H}\rangle$.

$$\langle\hat{H}\rangle = k_B T + \frac{\hbar^2 Q\eta}{2m\omega_0} \tag{2.18}$$

where Q is the quality factor of the system. It is clear that the mean energy consists of the expected thermal term $k_B T$ and an additional term which causes a temperature increase of

$$\Delta T_{\text{CSL}} = \frac{\Delta E_{\text{CSL}}}{k_B} = \frac{\hbar^2 Q\eta}{2k_B m\omega_0} \tag{2.19}$$

[11]

## 2.2 Mechanical resonator

Now let us focus on the actual movement of the mechanical resonator, i.e. the cantilever. We use the cantilever as a force sensor.



Version of August 8, 2025– Created August 8, 2025 - 13:34

### 2.2.1 Cantilever transfer function

To be able to analyse the force acting on the cantilever, we will need to know the transfer function on it:

$$H(\omega) = \frac{X(\omega)}{F_{ext}(\omega)} \tag{2.20}$$

Where $X(\omega)$ is the frequency dependent displacement of the cantilever and $F_{ext}$ any external force driving the cantilever. To determine the transfer function we use the equation of motion of a generic oscillator.

$$m\ddot{x} = -kx - c\dot{x} + F_{ext} \tag{2.21}$$

$m$ is the mass of the resonator, $k$ is the spring constant and $c$ is a constant of proportionality. $m$ and $c$ are combined in the parameter $\gamma = \frac{c}{2m}$ which is the damping factor. [13]. If we rewrite equation 2.21 to the frequency domain and plug it in equation 2.20 we obtain the following:

$$H(\omega) = \frac{1}{k - m\omega^2 + i\omega c} \tag{2.22}$$

The cantilever will be driven by a noise source. To see it's effect, we multiply the noise spectrum with the absolute square of the transfer function $|H(\omega)|^2$.

$$S_x(\omega) = |H(\omega)|^2 S_F(\omega) \tag{2.23}$$

$$|H(\omega)|^2 = \frac{1}{(k - m\omega^2)^2 + c^2\omega^2} \tag{2.24}$$

To find the average displacement as a result of any force noise $S_F(\omega)$ acting upon the cantilever, we multiply the force noise spectrum with equation 2.24 and integrate over all frequencies:

$$\left\langle \frac{1}{2}kx^2 \right\rangle = \frac{1}{2}k \int_{-\infty}^{\infty} x(t)^2 dx = \frac{1}{2\pi} \int_0^{\infty} S_x(\omega) d\omega = \frac{1}{2\pi} \int_0^{\infty} |H(\omega)|^2 S_F(\omega) d\omega \tag{2.25}$$

$$\langle E_{cantilever} \rangle = \left\langle \frac{1}{2}kx^2 \right\rangle \tag{2.26}$$

We have written the the expression in terms of the square of the displacement as the energy of the cantilever scales with it. [14]

### 2.2.2 Thermal motion

Now let us look at the effect of thermal noise on the movement of the cantilever. The thermal force noise spectrum is given by

$$S_{F,thermal}(\omega) = \frac{4k_bT}{\omega}\mathrm{Im}\left(\frac{F_{ext}}{X(\omega)}\right) = 4k_BT\gamma \tag{2.27}$$

Thermal noise is white, as it is not dependent of $\omega$. We now substitute eqation 2.27 into equation 2.23. This yields the following expression

$$S_{x,thermal}(\omega) = \frac{4k_BT}{m}\frac{\frac{\omega_0}{Q}}{(\omega_0^2-\omega^2)^2+\left(\frac{\omega_0\omega}{Q}\right)^2} \tag{2.28}$$

We have made some substitutions. Firstly the resonance frequency $\omega_0 = \sqrt{\frac{k}{m}}$ is substituted in. Furthermore the quality factor $Q = \frac{\sqrt{km}}{\gamma}$ is used. For high Q-factors and frequencies close to resonance ($\omega \approx \omega_0$) the distribution in equation 2.28 can be approximated as a Lorentzian distribution:

$$S_{x,thermal}(\omega) = \frac{k_BT}{k}\frac{\frac{\omega_0}{Q}}{(\omega_0-\omega)^2+\left(\frac{\omega_0}{2Q}\right)^2} \tag{2.29}$$

Lastly, when equation 2.29 is plugged into equation 2.25, the outcome confirms that the thermal motion of the cantilever satisfies the equipartition theorem

$$\left\langle \frac{1}{2}kx^2 \right\rangle = \frac{k}{4\pi}\int_0^\infty S_{x,thermal}(\omega)d\omega = \frac{1}{2}k_BT \tag{2.30}$$

Here we assume that the cantilever can only move in one dimension.[15]

## 2.3 SQUID thermometry

As stated in the introduction, the temperature of the setup is measured using a SQUID. The technical term for the kind of thermometer used is a magnetic flux fluctuation thermometer (MFFT)[16]. Let us look at the underlying theoretical principle.

### 2.3.1 MFFT

Johnson noise is the electronic current noise present in all electrical conductors and is the result of Brownian motion of the charge carriers in the

conductor.[17] This current noise induces a magnetic field in the material and therefore a flux noise spectrum $S_\Phi$. The power spectral density (PSD) of the flux noise of a conducting wire has the following expression:

$$S_\Phi = 4k_B T\sigma\mu_0^2 R^3 G(R/\delta) \tag{2.31}$$

where $\sigma$ is the bulk conductivity, $R$ is the radius of the wire, $T$ its temperature and $\mu_0$ the magnetic permeability of the conductor. $G$ is a dimensionless function dependent on the exact geometry of the MFFT. Two properties of $S_\Phi$ are important for the use as a thermometer. First, the flux noise produces a white spectrum as there is no dependence on the frequency of the noise $\omega$. Secondly, there is a linear dependence on the temperature $T$. For a more detailed look into the transfer function of the thermometer we refer to Van Heck et al. [16].

Chapter 3

# Setup and measurement method

In this chapter we will discuss the experimental setup and measurement methods of both the ultra low temperature cantilever measurements (Fermat) and the test measurements for the SRON detection chips.

## 3.1 Fermat

### 3.1.1 Experimental setup

The Fermat experiment is placed in a dry dilution refrigerator called *YETI*, a picture of which is shown in figure 3.1a. For a detailed explanation on the setup of *YETI* see ref [18]. On the still plate, a nuclear demagnetization stage (NDS) is mounted to cool the sample down sub 10 mk temperatures. This NDS consists of a superconducting coil. Within it's borehole a $PrNi_5$ matrix is placed. Through the coil a current is sent to generate a strong magnetic field, with a maximum field strength of 2T corresponding to a current of 40A. The matrix is thermalized to the mixing chamber (MC) plate with an aluminum thermal switch. Aluminum loses its thermal conductivity when in a superconducting state, therefore we are able to switch between a high and low heat conductivity by breaking the superconducting state of the aluminum. When ramping op the NDS coil, the generated field will align the spins in the $PrNi_5$ matrix, therefore lowering the entropy and increasing its temperature. This generated heat is able to flow to the MC-plate through the opened heat conductance switch. When the magnetized $PrNi_5$ matrix reaches the temperature of the MC-plate, the heat switch is closed and the magnetic field will be ramped down. When the field strength decreases the spins in the matrix disalign, raising the en-

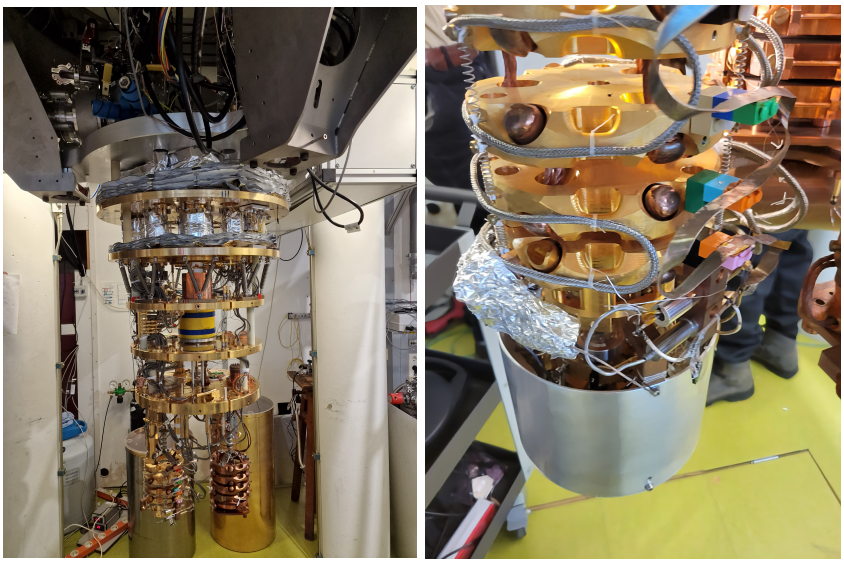

***(a)*** *Overview YETI* ***(b)*** *Close-up*

***Figure 3.1:*** *Overview of YETI and close up of the experimental setup. The blue and yellow object visible in the overview is the NDS coil. The silver wire originating from the coil can be seen attached to the mass spring system with Lego® blocks on the close-up photo.*

tropy. This causes the temperature of the matrix to drop and therefore the temperature of the silver wire it is soldered to. This silver wire extends down to the experiment.[19]

Underneath the MC plate the MRFM setup is suspended using a mass spring system (figure 3.1b. This mass spring system (figure 3.1b) consists of four copper masses and is optimized for filtering out mechanical vibrations between 100 Hz and 10 kHz. For the exact specifications of the mass spring system we refer to ref [20]. The cantilever used is an IBM-style silicon cantilever with a $Nd_2Fe_14B$ magnet attached to its tip. The magnet weighs an approximate of 1.5 ng. The cantilever has a resonance frequency $f_0$ of approximately 653 Hz and a stiffness $k \approx 2.6 \times 10^{-5}$ N/m.[18] A dither piezo is placed on the cantilever holder to drive the cantilever. The plate to which the cantilever is attached can be moved and positioned using three stick-slip piezo motors. These motors are positioned in a triangle. By extending and contracting the motors separately or together the piezo can be moved in $x$, $y$, and $z$. The position of the cantilever is measured and calculated using capacitors. A 2D sketch of the positioning system is shown in figure 3.2

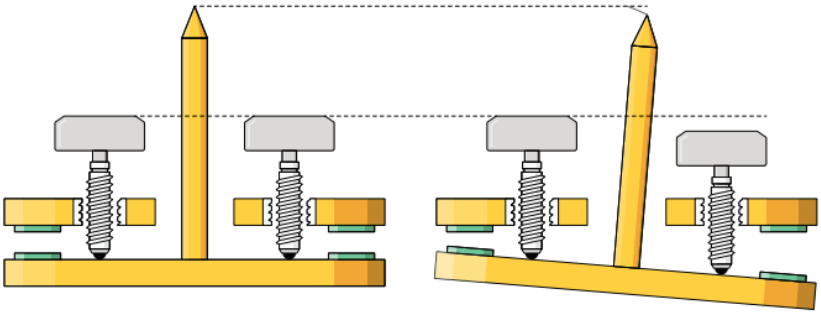

***Figure 3.2:*** *2D sketch of the positioning system of the cantilever. The cantilever is attached to the bottom. When extending both the piezos the plate moves downwards. When extending only one the cantilever is moved laterally. The green parts are the capacitor plates used in the position calculation. Sketch by J. Plugge [18]*

To detect the movement of the cantilever a detection chip is used. This chip is made of a commercially available $2.6 \times 2.6 \times 0.3$ mm$^3$ diamond plate. On the surface two pick-up loops made of niobium titanium nitride (NbTiN) are fabricated. Additionally an RF trace is fabricated, which we did not use for the measurements. The magnet on the tip of the cantilever induces a current through the superconducting loops given by

$$I = \frac{\Phi}{L} \tag{3.1}$$

Where $\Phi$ is the total flux through the surface enclosed by the loop and $L$ is the inductance of the loop. The alternating current induced by the movement of the magnetic tip is measured using a SQUID. In between the pick-loop and SQUID a transformer is used to improve the match between the inductance of the pick-up loop and the input coil of the SQUID. Lastly, after the transformer, a calibration coil is present that can be used to inject flux in the circuit and magnetically drive the cantilever. The pick-up loops, transformer and SQUID are all fabricated on separate chips. These chips are connected using wirebonds.

Both the cantilever and the detection chip are thermalized to the silver wire extending from the NDS coil. The temperature of the silver wire is measured using two kinds of thermometers. Firstly, We use two resistive thermometers made in house by W.A. Bosch. These thermometers are calibrated and known to be very precise until approximately 20 mK. To accurately measure temperatures below 20 mK, a MFFT is used. The MFFT

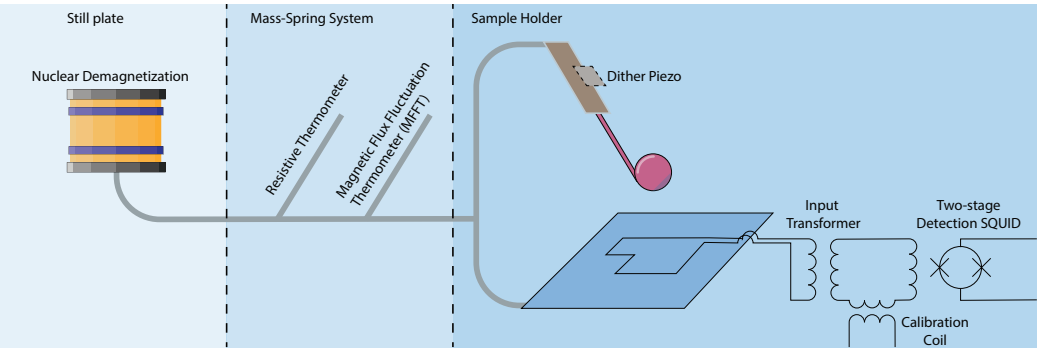


***Figure 3.3:*** *Schematic overview of the entire Fermat setup. From left to right: the NDS coil from which the silver wire extends. Then at the mass-spring system the silver wire splits to the resistive thermometer and MFFT. In the sample holder again the wire splits and thermalizes both the cantilever and the detection chip. Lastly, the detection circuit is shown. Figure is made by Ir. L.R. van Everdingen.*

consists of a gradiometrically wound coil around the silver wire and a SQUID. The coil picks up the flux fluctuations caused by Johnson noise described in section 2.3.1 which are then measured by the SQUID. The coil and SQUID are encased in a lead tube to minimize noise from stray magnetic fields. A schematic overview of the entire setup can be seen in figure 3.3

### 3.1.2 Methodology

We start the measurements by cooling down the setup in the *YETI*. During this cooldown the cantilever is retracted from the detection chip. This is done to prevent the cantilever crashing into the chip and damaging either the cantilever or the chip due to thermal shrinkage. When the cryostat has cooled down, we use the three piezo motors to gradually position the cantilever at the location where the coupling between the cantilever and the pickup loop is at its largest. In other words, the location where the movement of the cantilever generates the largest signal in the detection SQUID. We measure this coupling by moving the cantilever some distance and afterwards doing a frequency sweep using the dither piezo. We then fit a Lorentzian over the resonance peak. From this fit we can deduce the Q-factor and the amplitude. The arbitrary number Q/A is an indicator for the coupling: if Q/A increases, the coupling increases. To find an exact number of the coupling, namely the amount of voltage generated by a displacement of a meter of the cantilever, we use the calibration coil to magnetically sweep the cantilever.

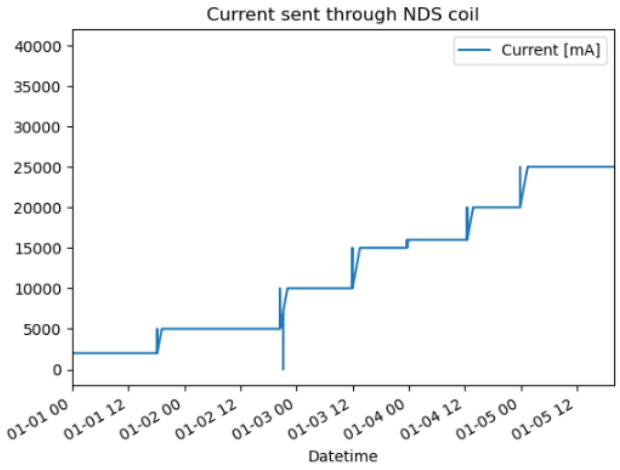


***Figure 3.4:*** *Current log of a measuring run. The lowest current corresponds to a temperature of ∼6 mk. The highest current corresponds to ∼40 mk. The spikes just before and after ramping up the current are caused by glitches in the Labview code.*

When the cantilever is positioned optimally, we start to cool down using the NDS stage. We follow the steps described in the section above. First we ramp up the field with the thermal switch opened. Then we close the switch and turn off the field to cool down the cantilever to sub 10 mk temperatures. When we have reached the lowest temperature possible, we ramp up the field again in steps. By doing this we heat up the cantilever again and create clear steps in temperature. We use these steps lasting a few hours to do energy analysis (see section 4). In figure 3.4 the current sent through the NDS coil for a measurement run can be seen. During these temperature steps we do additional magnetic sweeps to get a clear number for the coupling for each step. After measuring these steps, the setup is heated using a heater to around 150 mk. After this the heater turned off and the setup is allowed to gradually cool down again using the cooling of the refrigerator. This creates a gradual decrease in temperature and is used for calibration purposes for the MFFT. During the cooling and heating process the movement data from the detection SQUID is saved in TDMS files each containing 125 seconds of data. The sampling frequency is 250000 resulting in $3.125*10^7$ samples per file. The data from the MFFT is also saved in TDMS files as a voltage with a frequency of 50000 samples per second. Each file spanning 61 seconds resulting in $3.05*10^7$ samples per file.

## 3.2 SRON detection chips

### 3.2.1 experimental setup

The detection chips tested are an upgrade from the chips used presently in the FERMAT setup. They are fabricated by Space Research Organization Netherlands (SRON). The one major difference is the integration of transformers on the same chip as the pickup loop. This eliminates the need for the dedicated transformer chip now present in the setup and therefore two sets of wirebonds. This greatly lowers the parasitic inductance caused by the wirebonds between chips and potentially increased the coupling between the cantilever and the SQUID by an order of magnitude. The chips are made of isolating $SiO_2$ layers of 250 nm and three NbTiN conducting layers. The bottom two layers are 200 nm thick and the upper layer 500 nm. There are two pickup loops fabricated in the top layer. One has a notch in it (figure 3.5c). This is done to minimize the flux through the pickup loop caused by the RF line through the loops (red horizontal line in figure 3.5a and 3.5c). The rectangular pickup loop is $20 \times 30$ $\mu$m and has an inductance of 54 pH. A multilayer on chip transformer (rigure 3.5d) is connected to both pickup loops. The primary coil has one turn and an inductance of 0.251 nH. The secondary coil has 45 turns and an inductance of 388 nH. There are two test structures present on the chips. The first is a additional separate transformer identical to the ones connected to the pickup loops to test the transfer function of the transformers. The other structure can be used to test the inter-layer connections.

We primarily wanted to test whether the pickup loops worked. For this we had to place a local magnetic field over the loops and measure their response. We designed a sample holder for this purpose. It consists of a metal slab in which a flux concentrator coil perfectly fits. This coil uses the Meißner effect to concentrate the generated magnetic flux. For a more detailed explanation of how these coils work we refer to [21]. Above the coil a slot is cut out in which a PCB (printed circuit board) can be placed. The chip is glued on the PCB in such a way that the pickup loops are positioned above the core of the flux concentrator. The PCB is fastened on the sample holder using copper tape. The flux concentrator coil is wound with 100 $\mu$ NbTi/CuNi wire and has 105 windings. At room temperature

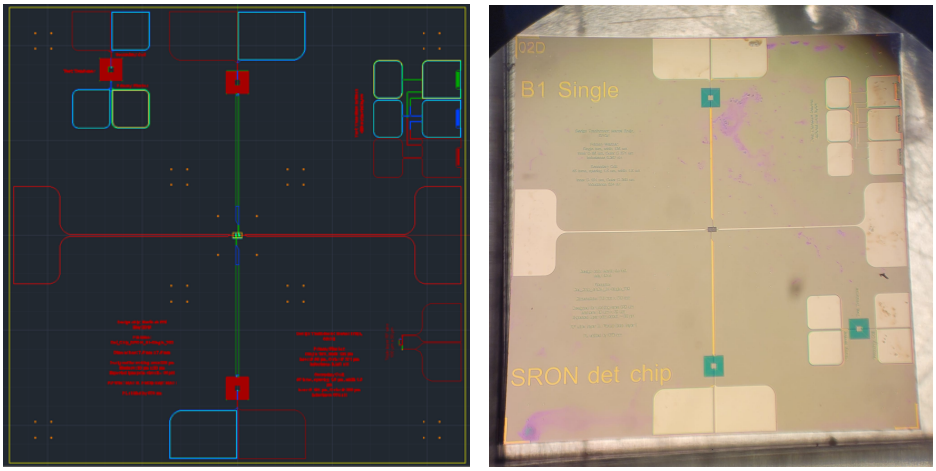


***(a)*** *Design chip* ***(b)*** *Photo chip*

***(c)*** *Pickup loops* ***(d)*** *On chip transformer*

***Figure 3.5:*** *Overview of the design of the SRON detection chips (a) and a picture of the chips under a microscope (b). In the middle of the chip two pickup loops are present (c). The transformers (d, red rings on the design) are placed at the edges of the chip. Additionally there are some test structures fabricated on the chip visible. The test transformer is placed differently on the actual measured chip than shown on the design.*

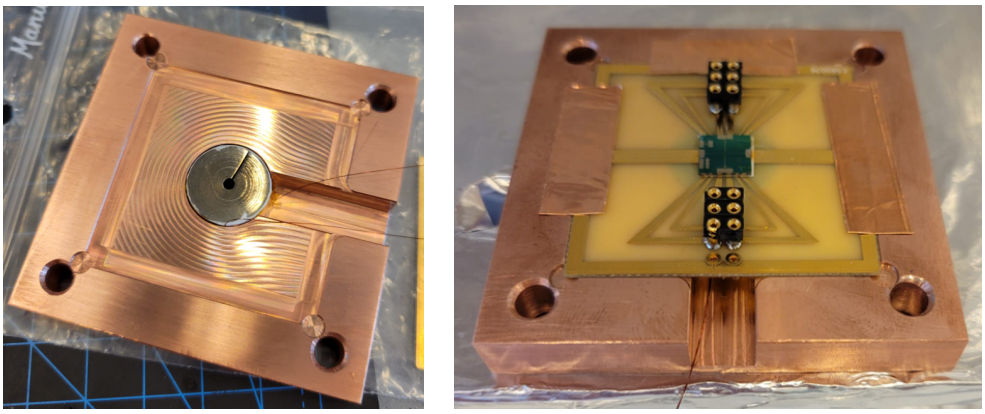

***(a)*** *Without PCB* ***(b)*** *With PCB*

***Figure 3.6:*** *Photos of the chip test sample holder without the PCB and the flux concentrator coil visible (a) and with the PCB on the sampleholder (b). The chip is glued on the PCB but the wirebonds are not yet placed between the chip and the PCB.*

the coil has a resistance of 19.9 Ω and an inductance of 85 $\mu$m. Four pins are soldered to each wire of the coil to increase the total current which can be sent. In figure 3.6 pictures of the sample holder can be seen.

We also wanted to test the pickup loops with a magnetic field coming from above the chip, as it would be in the actual MRFM setup. For this purpose we designed an additional construction and coil. As an additional flux concentrator coil could not be used, the designed coil had to be as narrow as possible to generate a sufficiently concentrated field. To do this, we designed a copper bobbin with a core of varying width. On one side, the core was 4 mm wides such that the bobbin could be screwed on a 2 mm wide screw. Along 2 mm the width of the core reduces to 2 mm forming a conical shape. The bobbin is screwed on a screw which is screwed in a copper plate. This plate is placed above the sample holder using three poles. The screw can then be turned to gradually lower the coil until it as close as possible to the chip. It ended up 12.3 mm above the chip. The coil is wound with the same wire as the flux concentrator coil. It has 464 windings, a resistance of 22 Ω and an inductance of 198 $\mu$H. Just like the flux concentrator, there are multiple pins soldered to the endings of the wire to increase the total possible current, only with this coil only two pins are used to each side. This is done to simplify the soldering and for spatial reasons. A photo of the complete setup including the top coil is visible in figure 3.7.

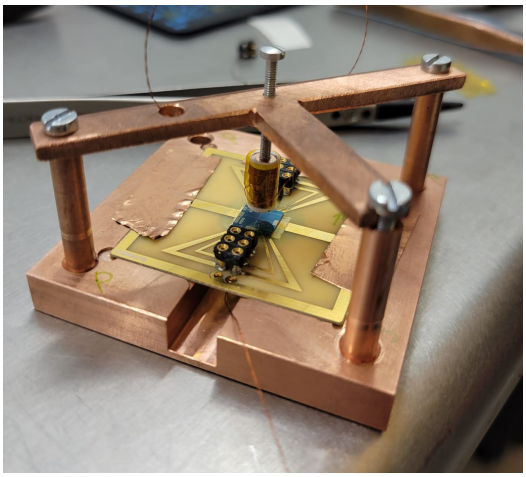

***Figure 3.7:*** *Photo of the complete sample holder*

### 3.2.2 Methodology

The NbTiN layers in the chip are expected to have a critical temperature $T_c$ of 11.8 K[22]. The niobium core of the flux concentrator has a slightly lower $T_c$ of 9.46 K[23]. Lastly, the NbTi wires have a $T_c$ of 10 K[24]. To reach these temperatures the experimental setup is placed in the dry dilution refrigerator *Elsa*. The sample holder is placed and screwed tightly to the still plate. This plate has a temperature of 1 K and is therefore more than cold enough to ensure the tracks, wires and core in the setup become superconducting.

As stated before, we mainly want to test the current response of the pickup loops when a magnetic field is sent over it. Equation 3.1 implies that a constant field generates a constant current. Therefore we send a constant current through the used coil (either the flux concentrator or the top coil) using the offset of a Zürich Instruments HF2LI lock-in amplifier. For the measurements with the flux concentrator we used four parallel wires, for the top coil measurements only two. To measure the generated current, we used a 1 kΩ resistor to convert the current to a voltage. This voltage was measured using a Keithley 2100 digital multimeter. As each wire in the cryostat can safely handle 10 mA, we can send at most 20 mA of current to the top coil. We match this maximum current with the flux concentrator to easily compare the two results. We ramp up the current from 0 mA to approximately 20 mA in 12 steps and measure the voltage over the resistor. For each amount of current we send we take 30 individual measurements spaced 20 ms apart. We then take the mean and standard

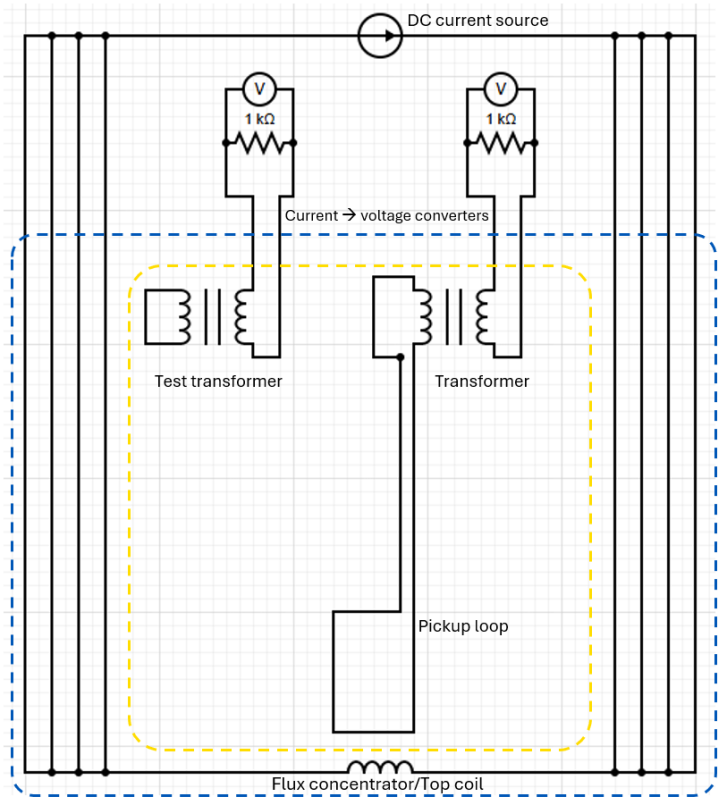


***Figure 3.8:*** *Schematic drawing of the measuring circuit used for the detection chip test measurements. The blue dotted line indicates which the components inside the cryostat. The yellow dotted lines indicate which components are part of the detection chip. Note that when using the top coil to measure only 2 wires are used as opposed to the four wires shown.*

deviation of these thirty measurements. We do this for both the regular and the notched pickup loop and for the test transformer we have shorted with itself. We then compare the results of the pickup loops and the test transformer to check wether the measured current is induced in the pickup loops or in the transformer also present in the pickup circuit. A schematic drawing of the measuring circuit is visible in figure 3.8

Chapter 4

# Analysis

The Fermat measurements described in section 3.1.2 gather a lot of data (15 terabytes), but before any conclusions can be drawn, this data needs to be analyzed. First, we look at the calibration of the MFFT. Secondly, the analysis of the thermal motion is described and lastly the two methods of Q-factor calculation are discussed.

## 4.1 MFFT

We start with the time dependent flux noise. As described in equation 2.31, the temperature dependency regards the PSD. For the time dependent flux noise to go to the PSD, we first take the Fourier transform of the flux noise. For each TDMS file a power spectrum is created (figure 4.1. The voltage noise is converted to flux noise i.e. the number of flux quanta. The noise is generally frequency independent as expected from equation 2.31. At higher frequencies, we do see the PSD decreasing. This is due to some unknown capacitance in the setup creating a low pass filter. In the otherwise smooth spectrum there are clear interference peaks visible. We can safely assume these are non-thermal and therefore we can filter these out. We did this by creating a mask: a selection of frequencies we did not use for the temperature analysis. We used the find_peaks function from scipy.signal to find the indices of the peaks. We did this for every spectrum. If a peak was present in more than 1.5% of the spectra, the frequencies corresponding to the peak were discarded. This resulted in a mask used for all spectra. The mask discards 16.1% of the data.

After obtaining the masked spectra. We integrated the clean spectra to

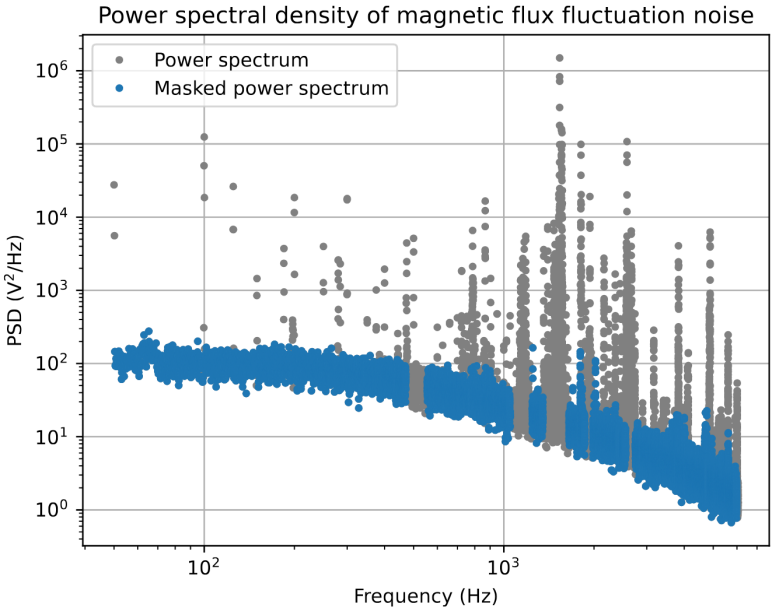


***Figure 4.1:*** *$S_\Phi$ of the MFFT at one point in time. The gray spectrum is the spectrum before the mask got applied to it. The blue spectrum is the masked spectrum used for the temperature analysis*

find the total noise power each timestep. As we do not precisely know the conductance $\sigma$ and the geometric term $G(R/\delta)$ in equation 2.31, we cannot use the integrated power to calculate the temperature. To obtain the temperature as function from the flux noise, we calibrate the MFFT using the resistance thermometers present in the setup. We do this by fitting a linear function to the integrated power as a function of the temperature of the resistance thermometers. We use the gradual decrease in temperature from 150 mk described in section 3.2.2 (figure 4.2). The fit parameters are then applied to all the calculated integrated power values to find the temperature for every point in time. As is visible in figure 4.2, two resistance thermometers are installed in the setup. For the calibration we use thermometer M.

We are especially interested in the temperature on the discrete temperature steps created by ramping the NDS coil up in steps. From each step we defined a period of two hours on which the temperature was stable. We made a histogram of the temperatures at different times within this period. The temperatures in this period were normally distributed. To find the average temperature and the standard deviation we first normalized the histogram by dividing it by the total amount of counts. After this

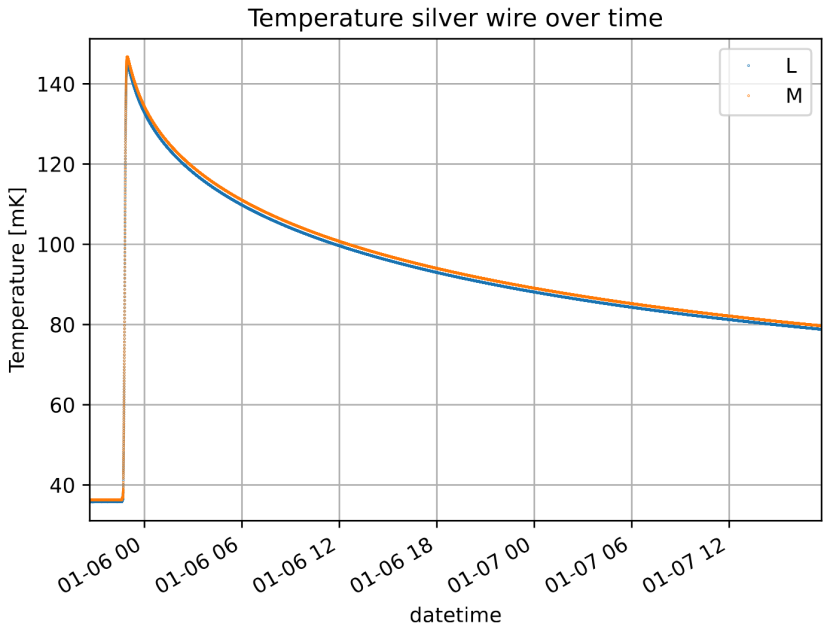


***Figure 4.2:*** *Used calibration slope for the MFFT. The two resistance thermometers are referred to as L and M*

we fitted a Gaussian over the normalized histograms:

$$f(x) = \frac{1}{\sqrt{2\pi\sigma^2}} e^{-\frac{(x-\mu)^2}{2\sigma^2}} \tag{4.1}$$

where $\sigma$ is the standard deviation and $\mu$ the average.

## 4.2 Thermal motion

To study the thermal motion we first needed to find the energy of the cantilever. We do this by applying a digital lock-in amplifier to the SQUID data to separate the real and imaginary part of the signal. The lock-in is applied at the resonance frequency. This resonance frequency is found by fitting a Lorentzian to the data, as the thermal motion takes the shape of a Lorentzian (equation 2.29). We use a Butterworth filter with a cutoff frequency of 0.5 Hz to filter out the secondary peak resulting from the lock-in. Lastly, we multiply the resulting values with a conversion factor of 2*$10^{-5}$ m/v to get the displacement $x$. These values are then plugged in equation 2.30 to ultimately find the energy of the cantilever. This conversion factor is found using magnetic sweeps with the calibration coil. For the exact

method of finding this conversion factor we refer to [18]. The energy analysis is done in the same manner for frequencies 5 Hz above and below the resonance frequency. This is done to obtain the energy background.

## 4.3 Q-factor

We used two methods for obtaining the Q-factor of the cantilever. Firstly, the Q-factor is calculated using the Lorentzian fit done to find the resonance frequency. The Q-factor can be calculated by dividing the resonance frequency with the full width half maximum (FWHM). The second method is by using the autocorrelation function. The Q-factor is a measure for how fast the cantilever loses its energy, a higher Q-factor means that the cantilever loses its energy more slowly. For high Q the autocorrelation is therefore high. The autocorrelation can be calculated using the following formula:

$$R(t_2) = \langle (E(t_1) - \bar{E})(E(t_1 + t_2) - \bar{E}) \rangle \tag{4.2}$$

$\bar{E}$ is the average energy. The autocorrelation exponentially decays characterized by a correlation time $\tau$:

$$R(t_2) \propto e^{\frac{-2t_2}{\tau}} \tag{4.3}$$

Q can then be calculated using $\tau$:

$$Q = \frac{\omega_0 \tau}{2} \tag{4.4}$$

Where $\omega_0 = 2\pi f_0$. After this exponential function is fitted to the autocorrelation. The first $\frac{1}{f_c} = 2$ seconds are not used for the fit as the low-pass filter of the lock-in causes the autocorrelation to increase in this regime.[14].

Chapter 5

# Results

## 5.1 Fermat

In this section we will discuss the results of run 73 of the Fermat experiment. We will look at the temperature of the sample measured with the MFFT and the energy and temperature of the cantilever using its thermal motion. Lastly, we will discuss the Q-factor of the cantilever. We will then combine all results and discuss the implications on the upper bounds of CSL parameters.

### 5.1.1 MFFT

First let us look at the temperature of the sample measured using the MFFT. The linear fit described in section 4.1 is shown in figure 5.1. The resulting fit function is $\int S_\Phi df = 2.3 \cdot 10^4 * T + 7.3 \cdot 10^3$. As you can see, the function is now in the form of $\int S_\Phi df = aT + b$. As we want to find the temperature as a function of the flux noise, we invert the function to $T = \frac{\int S_\Phi df - b}{a}$. We apply the found expression for the temperature to all the values of the integrated power. This then gives us the temperature for all points in time. A plot for the temperature over time including the discrete temperature steps is visible in figure 5.2. As you can see, the temperature given by the MFFT and the two resistance thermometers deviate significantly from each other at low temperature. There are a number of peaks visible in the temperature given by the MFFT. These are not present in the temperature given by the resistance thermometers and are therefore most likely caused by non-thermal resonance effects at that point in time.

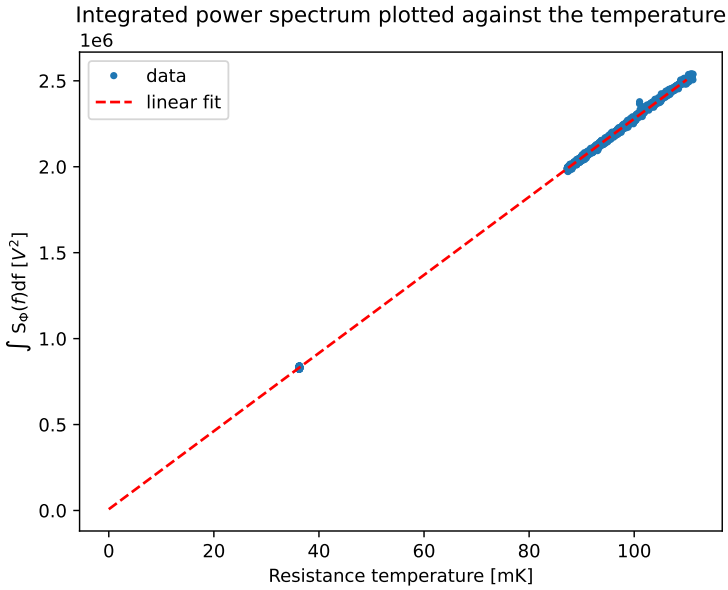


***Figure 5.1:*** *The integrated power spectrum of the silver wire plotted against the temperature measured by the resistance thermometer. The linear fit is described by the function* $\int S_\Phi df = 2.3 \cdot 10^4 * T + 7.3 \cdot 10^3$*. This equation implies that there is noise present at* $T = 0$*, but this is wrong. We will go further into this in the discussion (section 6).*

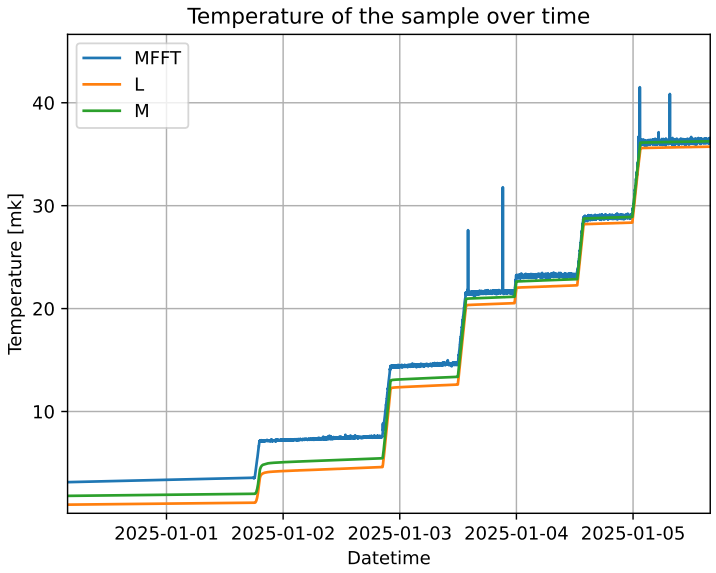


***Figure 5.2:*** *Temperature over time during a stepwise NDS ramp.*

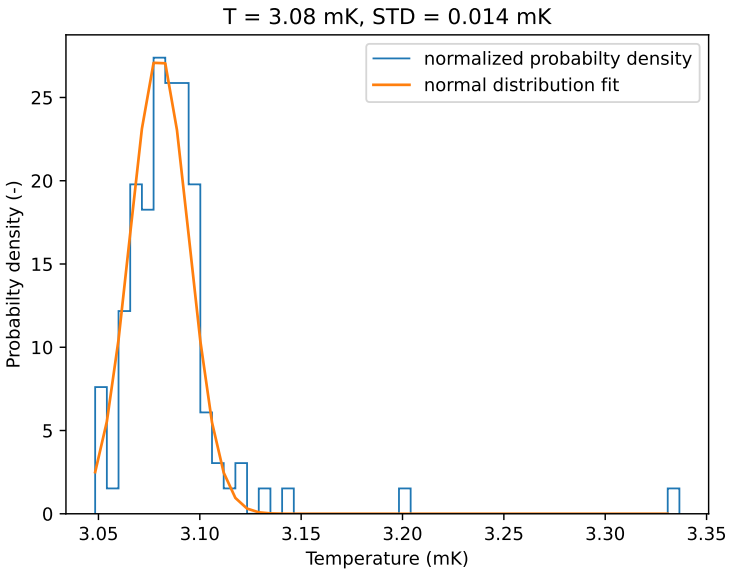


***Figure 5.3:*** *Temperature histogram of the lowest temperature reached. The Gaussian fit is done using equation 4.1 The average temperature and standard deviation are visible in the title of the plot.*

Now, as described in section 4.1, we found the average of the temperature during the steps and the corresponding standard deviations by fitting a Gaussian over the normalized histograms of the temperature during the steps. The temperature histogram of the lowest reached temperature is visible in figure 5.3, the histograms of all other steps are shown in the appendix. The lowest temperature reached during this NDS run is 3.08 mK. As expected, the standard deviation of the temperature rises along with the temperature itself.

### 5.1.2 Thermal motion

Now let us look at the thermal motion and temperature of the cantilever. We have found the energy of the cantilever over time using the digital lock-in described in section 4.2. To compare the temperature of the cantilever with the temperature of the sample during the steps, we analyze the energy during the same periods used for the MFFT histograms. Once again, we gather the found energies in histograms. The energies are described using the Boltzmann distribution (equation 2.30). The energy histogram of the lowest temperature reached is visible in figure 5.4, the his-

tograms of all other temperature steps are shown in the appendix. Along with the energy histogram, the Boltzmann distribution is plotted according to

$$y = Ae^{-E/k_bT} \tag{5.1}$$

$A$ is a scaling factor. In our case the height of the first bin in the histogram is chosen as $A$. The temperature is found using the average energy of the time period. The average energy is shown as a vertical black line in the histograms. The corresponding temperature is shown in the legend of each plot.

We now combine the results of the MFFT measurements and the thermal motion measurements into one plot (figure 5.5). Both the temperatures shown in figure A.2 are shown and the calculated temperatures where the energy background is subtracted. A linear fit is done over the temperatures with the background subtracted. As is visible, the data points quite clearly deviate from the fit at low temperatures. This could be caused by the noise floor preventing the cantilever from cooling down, but may also be due to a faulty calibration. The error in the cantilever temperature is calculated according to the formula

$$\sigma_T = \frac{\langle E \rangle}{K_b} * \sqrt{\tau N} \tag{5.2}$$

Where $\tau$ is the correlation time of the cantilever and $N$ the total number of measurements.

### 5.1.3 Q-factor

Lastly, let us look at the Q factor of the cantilever over time. One of the autocorrelation fits described in section 4.3 is shown in figure 5.6. For every energy calculation lasting 125 seconds an autocorrelation fit is done, but again, we are interested in the discrete temperature steps. The average Q-factor of each step is shown in figure 5.7. There is no clear relation between the Q-factor and the temperature visible for both the Lorentzian fit and autocorrelation Q-factors. The only clear difference between the two is that the autocorrelation Q-factor is consistently higher than the one obtained from the Lorentzian fit. However, the error margins of the autocorrelation Q-factors are very large, for the second temperature step even crossing over towards negative values. Therefore, we mainly trust the Lorentzian Q-factors as their error margins are much smaller.

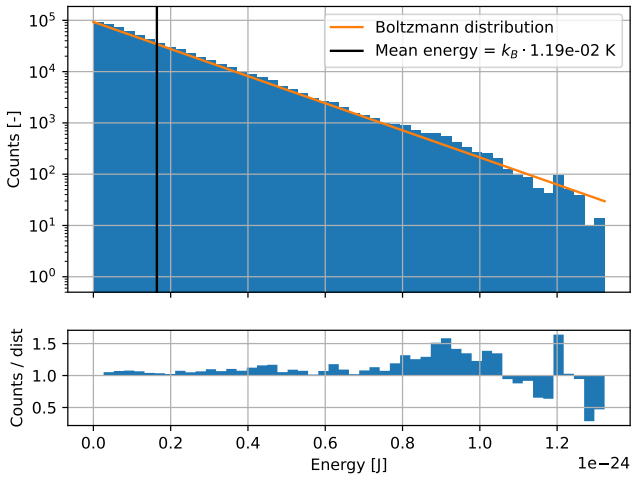


***Figure 5.4:*** *Energy histogram of the thermal motion at the lowest reached temperature of the cantilever. The histogram describes the same two hours as the temperature histogram in figure 5.3. The graph underneath the main histogram shows how much the energy distribution differs from the expected Boltzmann distribution.*

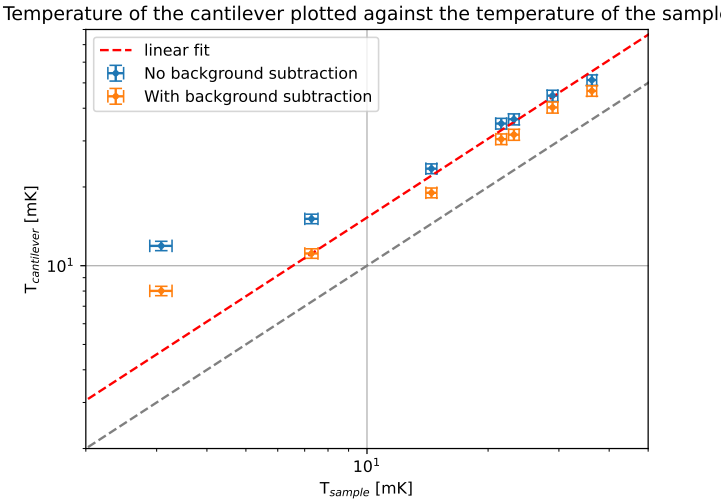


***Figure 5.5:*** *Temperature of the cantilever plotted against the temperature of the sample. Both the temperatures with and without the background are shown. The red dotted line is a linear fit done according to $y = ax$. This line is mainly present to clearly show the deviation from the trend for the lowest temperature. The grey dotted line represents the function $y = x$*

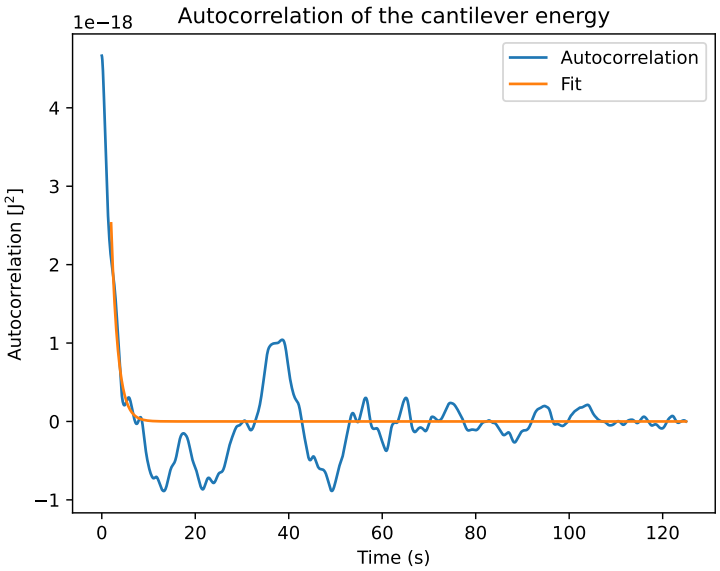


***Figure 5.6:*** *Autocorrelation of the energy of the cantilever at one point in time. The exponential fit over the autocorrelation is shown in orange. As described in section 4.3, the first two seconds of the data is not used for the fit. The Q-factor obtained from this particular fit is 6035.2. The Q-factor obtained from the Lorentzian fit over this data is 5524.0*

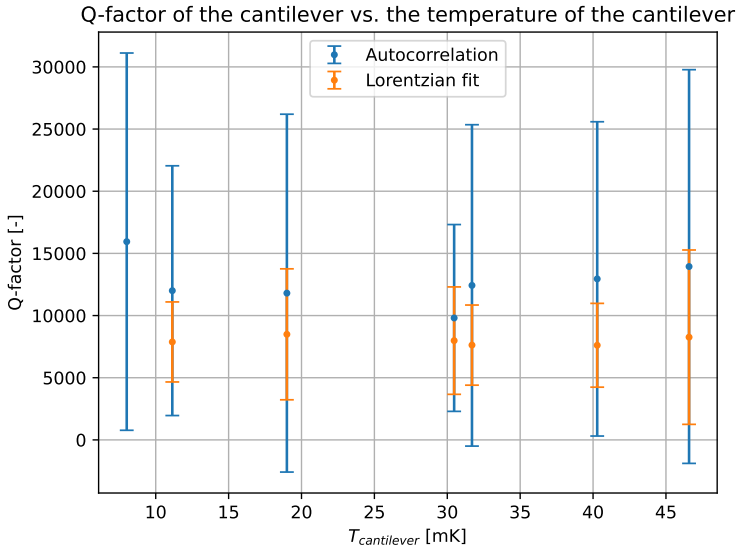


***Figure 5.7:*** *Average Q-factor of the cantilever obtained from the Lorentzian fit and autocorrelation during the analyzed periods during the discrete energy steps. The Q-factor of the period during the lowest temperature obtained from the Lorentzian fit is missing, as there was no fit data of that period available.*

### 5.1.4 CSL upper bounds

We will now use the discussed results to calculate the implications for the upper bounds for the CSL parameters. As the noise created by CSL manifests itself as force noise, we will first calculate the force noise on the cantilever according to the following formula:

$$\sqrt{S_F} = \sqrt{\frac{4k_B T k}{\omega_c Q}} \tag{5.3}$$

We insert the values found during the lowest temperature reached in the formula: $T = 8$ mK, $\omega_c = 2\pi f_c = 2\pi * 669$ Hz, $Q = 1.6 \cdot 10^4$. For the stiffness of the cantilever $k$ we use $2.6 \cdot 10^{-5}$ N/m. This gives us $\sqrt{S_F} \approx 4.1 \cdot 10^{-19}$ N/$\sqrt{\text{Hz}}$. This value is in the same order of magnitude as earlier found values ($5 \cdot 10^{-19}$ N/$\sqrt{\text{Hz}}$ [25]). The figure of merit for CSL measurement is $S_F/R^2$ and as above value was found using a smaller cantilever, no improvement of the CSL parameters can be made.

## 5.2 SRON detection chip

Lastly we will discuss the results of the SRON detection chip test measurements. The results of the measurements using the flux generator sending a magnetic field from underneath the chip are visible in figure 5.8a. The positive relationship between the measured voltage and the sent current for both the regular and notched pickup loop implies the chips works as expected. Especially as the data from the test transformer shows no clear reaction from an increased magnetic field sent by the flux concentrator. The noise floor of the Keithley multimeter was approximately $9 \cdot 10^{-7}$ V, so almost an order of magnitude less than the measured signal from the regular loop.

The data behaves less predictably for the measurements using the top coil. As you can see in figure 5.8b, the data for the regular pickup loop behaves as expected and similar the corresponding data obtained using the flux concentrator. However, the notched coil shows a clear negative relationship between the measured voltage and magnetic field. This would imply a difference in polarity between the regular and notched coil. However, if we negate the current independent offset, the absolute value of the voltage has a positive relationship with the magnetic field over the pickup loop. The behavior of the data of the test transformer is quite strange. It almost shows an inverse exponential relationship with the sent field. We cannot explain this for now, as no equation implies this behavior. However, we can safely say that at least the regular pickup loop works as expected.

If we now look at equation 3.1, we can calculate the supposed flux through the pickup loop. A voltage of approximately 7.5 $\mu$V over a 1 k$\Omega$ resistance implies a current over the resistance of 7.5 nA. The current induced in the loop is attenuated by a factor 45 by the transformer (as the ratio between primary and secondary coil is 1:45). The current induced in the loop is thus 337.5 nA. This gives a total flux of $1.823 \cdot 10^{-17}$ Wb. This flux gives a flux density of approximately $3 \cdot 10^{-8}$ T. Theoretically, the flux concentrator coil generates a field of $23.25 \cdot 10^{-2}$ T at the center of the coil. This is approximately five orders of magnitude more than implied by the measured voltage. The value for the theoretical field strength is calculated using the model for an infinitely long solenoid. If we instead calculate the theoretical field using the equation for the magnetic field along the axis



Version of August 8, 2025– Created August 8, 2025 - 13:34

perpendicular to a current loop

$$B_z = \frac{\mu_0}{4\pi} \frac{2\pi R^2 I}{(z^2 + R^2)^{\frac{3}{2}}} \tag{5.4}$$

where $R$ is the radius of the loop and $z$ the distance from the center. The radius of the flux concentrator core is approximately 2 mm and for $z$ we also use 2 mm. This gives a field strength of approximately $2 \cdot 10^{-4}$ T. This is already quite a bit closer to the calculated field of $3 \cdot 10^{-8}$ T, but still 4 orders of magnitude bigger. The top coil produces a theoretical magnetic field of

$$B = \mu_0 \mu_{Cu} \frac{NI}{l} = 1.27 \cdot 10^{-3} \text{ T} \tag{5.5}$$

inside the coil, where $\mu_{Cu}$ is the magnetic permeability of copper. To calculate the field strength at the chip, we use the following formula:

$$B(z) = \frac{\mu_0 N I R^2}{2(R^2 + z^2)^{\frac{3}{2}}} \tag{5.6}$$

For $R = 2$ mm and $z$ = 12.3 mm the equation gives a field strength of approximately $1 \cdot 10^{-5}$ T. This, again is closer to the supposedly measured field but still 3 orders of magnitude too high. It does explain the lower signal measured when sending a field with the top coil as the field experienced by the pickup loops is lower then the field produced by the flux concentrator.

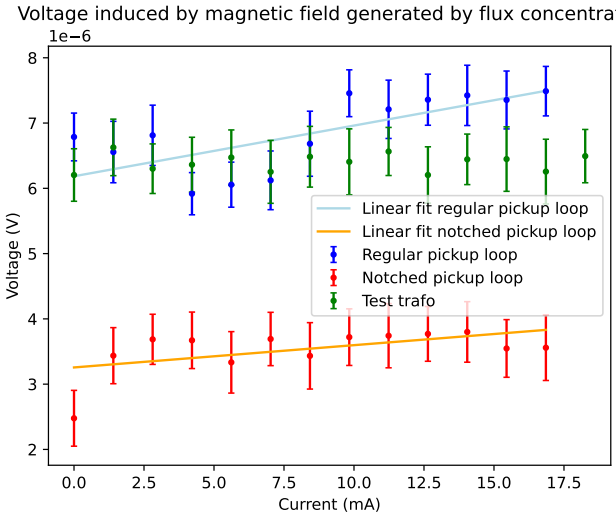


***(a)*** *Fit data regular loop:* $V = 7.77 \cdot 10^{-8} * I + 6.18 \cdot 10^{-6}$*, fit data notched loop:* $V = 3.41 \cdot 10^{-8} * I + 3.26 \cdot 10^{-6}$

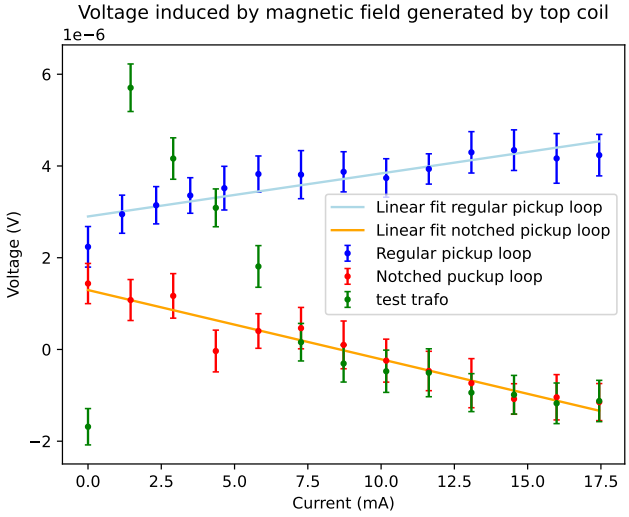


***(b)*** *Fit data regular loop:* $V = 9.39 \cdot 10^{-8} * I + 2.90 \cdot 10^{-6}$*, fit data notched loop:* $V = -1.51 \cdot 10^{-7} * I + 1.30 \cdot 10^{-6}$

***Figure 5.8:*** *Voltage over the 1 kΩ resistance in series with the pickup loop generated by the superconducting current induced by the magnetic field of the flux concentrator (a) and the top coil (b). The results for the test transformer are shown in green in both plots. The attribute the offset in all four fit functions to noise resulting from the multimeter and wiring of the cryostat.*

Chapter 6

# Discussion

Now that we have gathered all the results, let us critically discuss them. First we will look into the results of the Fermat experiment. Subsequently we will discuss the results of the detection chips and more importantly, whether they can be used in the Fermat experiment as detection chips for the movement of the cantilever.

## 6.1 Fermat

Despite gathering a lot of useful data, we have not managed to set new upper bounds for the CSL parameters. If we compare our results to the previous results of the Fermat experiment described in [16], we find two key differences, namely a difference in both reached temperature and Q-factor of the cantilever. We will discuss both aspects.

First let us look at the reached temperature of the sample. Van Heck et al. ([16]) claim they have reached a sample temperature of 1.5 mK. Significantly lower than our lowest reached temperature of approximately 3 mK. This might be explained by the analysis method, as the NDS stage setup has not changed. As explained in section 4.1, the non thermal peaks in the noise spectrum of the MFFT are masked. Van Heck et al. fill in the 'holes' created in the spectrum with white noise. We have chosen not to do this and discard the masked frequencies altogether. An additional reason our MFFT temperature is higher is because our mask leaves out too many non thermal peaks. As you can see in figure 4.1 there are still some unmasked peaks. These peaks raise the IPS and therefore the calculated temperature of the sample.

One solution to this problem would be to design a primary MFFT. This means that this thermometer does not need to be calibrated to a different thermometer as is the case in our setup right now. In a sense, the MFFT we now use can be used as a primary thermometer, provided we learn the exact geometry of the sensor such that we can fill in the geometric term in equation 2.31. However, this is unrealistic. In a paper written by Kirste and Engert ([26]) the design of a primary thermometer using the temperature dependence of the magnetic flux noise spectrum is discussed. This geometry of this thermometer is designed in such a way that the exact temperature dependence of the flux noise is known. Therefore, the temperature can be directly calculated from the measured flux noise. Furthermore, this thermometer uses two SQUIDS. These two SQUIDS produce two noise measurements which are then used to calculate a cross-correlated noise spectrum. The pickup coil of one of the SQUIDS is located directly above the temperature sensor of the thermometer while the pickup coil of the other SQUID is located far away from the temperature sensor. Combining the two signals of these SQUIDS for the cross-correlated noise spectrum filters out a lot of the non-thermal peaks we have to filter out. A different upgrade to the current MFFT would be a thermometer which uses the superconducting transition of a number of wires made from different metals. The materials we would use have a well known critical temperature. We then could calibrate the measured flux noise to these transition temperatures, eliminating the need for the calibration to the resistance thermometers. However, this does not solve the problem of the non thermal peaks. An upgrade to the MFFT where these peaks are filtered out like the thermometer in [26] would be a useful addition to the experimental setup.

In Van Heck et al. the temperature of the sample is used to calculate the force noise spectrum $\sqrt{S_F}$. We have used the temperature of the cantilever obtained from the thermal motion measurements. Unfortunately, there are no thermal motion measurements presented below 20 mK. Therefore we cannot clearly compare our obtained cantilever temperature at the lowest sample temperature to that of Van Heck et al. We can, however, compare the Q-factor of the cantilever. Van Heck et al. use the Lorentzian fit method to find the Q-factor. The Q-factor they found was with a value of 40000 a lot higher than the value we found using this method (approximately 8000). The Q-factor found using the autocorrelation fit was higher at around 16000, but we deem that method too unreliable. As is visible in figure 5.6, the error margin of the autocorrelation is very large. This is

caused by the fact that for quite a few points in time, the exponential fit was sufficient and gave an unrealistic value for Q.

One reason Van Heck et al. found a much higher Q-factor could be that the Q-factor measurements they did was not at same cantilever position as the thermal motion measurements. For the latter measurements the cantilever should be as close as possible to the sample, to pick up as much of the thermal motion. However, this does lower the Q-factor as the magnet on the tip of the cantilever couples to the spins in the sample and therefore restricting its motion. This is most likely also the reason the described trend in of the Q-factor (lower temperature leads to a higher Q-factor). The cantilever has to be this close to the sample because the low possible coupling between the cantilever and the SQUID. This is caused by the parasitic inductance of the wirebonds between the pickup-, transformer- and SQUID chip. The tested detection chips with the transformer on the detection chip could partly solve this problem by eliminating the need for one set of wirebonds.

## 6.2 SRON detection chips

The inclusion of the detection chips in the Fermat setup would be a great addition, provided they work as expected. The measurements done in this project shed some light on the usability of these chips much is still unclear. Although the expected positive relationship between the magnetic field and the measured voltage was found, the signal itself was weaker than expected according to equation 3.1. Both the theoretical field of the flux concentrator and the top coil was several orders of magnitude higher than the suggested field from the measurements. One possible explanation for the top coil is that it was not close enough to the chips. We lowered the coil as much as possible but due to the wirebonds of the chip to the PCB, we could not get the coil as close as we wanted.

Furthermore, the coil was not exactly centered above the pickup loops due to a fabrication error. We tried to compensate this by gluing the chip also slightly off-center, but we did not manage to exactly align the chip and top coil. This attempt of aligning the chip with the top coil inadvertently caused the chip to also be misaligned with the flux concentrator. We did not believe this to be a problem before the measurement, as earlier measurements with just the flux concentrator (but with a different chip of the same design) did not deliver usable results. Because of this we did not

believe the configuration with the flux concentrator would work.

This being said, we do believe the results point to the chips working as expected for DC fields. The measured noise floor of the multimeter is well below the measured signal so the change in measured voltage has to be caused by the growing magnetic field. Unfortunately, we could not gather such results for an AC field. As the chips would ultimately be measuring the magnetic field caused by the magnetic tip of the cantilever, we wanted to test the chip with an alternating field with a frequency of 700 Hz, approximately the resonance frequency of the cantilever. These attempts were not successful, because the multimeter was not sensitive enough to measure the AC voltage. Crude tests showed that the lowest AC voltage the multimeter could accurately measure was in the order of $10^{-4}$ V, two orders of magnitude larger than the expected signal. Before implementing the chip in the Fermat setup, we recommend to test the chip with an alternating field to confirm it would accurately measure the oscillating cantilever. This can be done with a more accurate multimeter but maybe even a SQUID, especially because a SQUID will be used to measure the signal of the cantilever in the Fermat setup. Additionally, we would doing other tests on the chip such as testing the critical current of the superconducting tracks, the conductivity between the three metal layers of the chip and the workings of the RF-line. These three tests are not essential for use in the Fermat setup, but teach us a lot about the workings of the chip.

Chapter 7

# Conclusion and outlook

In this thesis we have discussed the latest results of the Fermat experiment regarding the thermal motion of a mechanical oscillator at ultra low temperatures. The nuclear demagnetization stage works well in cooling down the cryostat to approximately 3 mk, much lower than the standard dry dilution cryostat temperature of approximately 20 mk. This temperature was accurately measured using a magnetic flux fluctuation thermometer (MFFT), a thermometer which uses the temperature dependence of Johnson noise. At these low temperatures we can accurately measure the thermal motion of the cantilever opens up the possibility in testing the continuous spontaneous localization model regarding the measurement problem within quantum mechanics. Furthermore, we have tested an shown promising results for a new measurement chip to be implemented in the current Fermat setup. This chip has pickup loops as well as a transformer on it, eliminating the need for a separate transformer chip and therefore additional wirebonds. The absence of the wirebonds and their parasitic inductance will greatly increase the coupling between the cantilever and the SQUID.

However, the results of the measurement run discussed in this thesis prove to be unusable to lower the upper bounds for the CSL parameters $\lambda$ and $r_c$. This is due to the fact that the cantilever did not reach the low temperature of the cryostat, but only reached a temperature of $\sim$ 8 mk, where previous exclusion calculations were done using a temperature of $\sim$ 1.5 mk. Additionally the measured Q-factor of the cantilever was too low ($\sim$ $10^3$ vs. $4{\cdot}10^3$) To improve these numbers in the future, we need to position the cantilever further away from the MRFM sample. For this to be feasible the new chip has to be installed, however much is still unknown about

the workings of the chip. We only managed to get results for a constant magnetic field, which, albeit promising, were not conclusive. Tests using an alternating field are necessary. Additionally, after the implementation of the SRON detection chips, designing and installing a primary SQUID thermometer less susceptible for non-thermal mechanical noise would be a great addition to the Fermat experiment.

# Acknowledgments

I would like the Oosterkamp group for the opportunity to work with and contribute to the Fermat project. I learned more about quantum mechanical research than I could have imagined at the start of the project. I felt trusted to figure things out on my own while still being able to ask any question I had. Many thanks to Tjerk for all the ideas and guidance. Many thanks to Loek for trusting me to handle ″serious″ tasks and letting me work alongside him on the project (and for being a very 'gezellig' colleague). Thanks to Mart and all the other students and PhD candidates in both the Oosterkamp and Hensen group in the new measurement hall for ensuring a nice work environment where there is always room for a nice chat besides the serious work.

# Bibliography


[1] M. Schlosshauer, *Decoherence, the measurement problem, and interpretations of quantum mechanics*, Reviews of Modern Physics **76**, 1267 (2005).

[2] M. Tegmark, *The Interpretation of Quantum Mechanics: Many Worlds or Many Words?*, Fortschritte der Physik **46**, 855 (1998).

[3] J. Faye, *Copenhagen Interpretation of Quantum Mechanics (Stanford Encyclopedia of Philosophy)*, 2024.

[4] G. C. Ghirardi, A. Rimini, and T. Weber, *Unified dynamics for microscopic and macroscopic systems*, Physical review. D. Particles, fields, gravitation, and cosmology/Physical review. D. Particles and fields **34**, 470 (1986).

[5] R. Frigg, *GRW Theory (Ghirardi, Rimini, Weber Model of Quantum Mechanics)*, 2009.

[6] G. C. Ghirardi, P. Pearle, and A. Rimini, *Markov processes in Hilbert space and continuous spontaneous localization of systems of identical particles*, Physical Review A **42**, 78 (1990).

[7] M. Bahrami, *Testing collapse models by a thermometer*, Physical review. A/Physical review, A **97** (2018).

[8] A. Bassi, K. Lochan, S. Satin, T. P. Singh, and H. Ulbricht, *Models of wave-function collapse, underlying theories, and experimental tests*, Reviews of Modern Physics **85**, 471 (2013).

[9] S. L. Adler and A. Bassi, *Is quantum theory exact?*, Science **325**, 275 (2009).

[10] R. P. Dobrow, *Introduction to Stochastic Processes With R*, 2016.

[11] A. Vinante, M. Bahrami, A. Bassi, O. Usenko, G. Wijts, and T. H. Oosterkamp, *Upper Bounds on Spontaneous Wave-Function Collapse Models Using Millikelvin-Cooled Nanocantilevers*, Physical Review Letters **116** (2016).

[12] M. Carlesso, S. Donadi, L. Ferialdi, M. Paternostro, H. Ulbricht, and A. Bassi, *Present status and future challenges of non-interferometric tests of collapse models*, Nature Physics **18**, 243 (2022).

[13] G. R. Fowles and G. L. Cassiday, *Analytical Mechanics*, Brooks/Cole Publishing Company, 1999.

[14] G. L. van de Stolpe, *Global Warming through Wave Function Collapse*, 2019.

[15] J. de Voogd, *MRFM and the Spin Bath*, 2018.

[16] B. Van Heck, T. M. Fuchs, J. Plugge, W. A. Bosch, and T. H. Oosterkamp, *Magnetic Cooling and Vibration Isolation of a Sub-kHz Mechanical Resonator*, Journal of Low Temperature Physics **210**, 588 (2023).

[17] J. F. Qu, S. P. Benz, H. Rogalla, W. L. Tew, D. R. White, and K. L. Zhou, *Johnson noise thermometry*, Measurement Science and Technology **30**, 112001 (2019).

[18] J. Plugge, *Probing the limits of quantum mechanics using a cold mechanical force sensor*, 2025.

[19] F. Pobell, *Refrigeration by Adiabatic Nuclear Demagnetization*, pages 215–258, Springer Berlin Heidelberg, Berlin, Heidelberg, 2007.

[20] M. De Wit, G. Welker, K. Heeck, F. M. Buters, H. J. Eerkens, G. Koning, H. Van Der Meer, D. Bouwmeester, and T. H. Oosterkamp, *Vibration isolation with high thermal conductance for a cryogen-free dilution refrigerator*, Review of Scientific Instruments **90** (2019).

[21] J. Plugge, *Generating High B0-fields for use in Extremely Low Temperature MRFM*, 2020.

[22] H. Machhadani, J. Zichi, C. Bougerol, S. Lequien, J.-L. Thomassin, N. Mollard, A. Mukhtarova, V. Zwiller, J.-M. GÃ©rard, and E. Monroy, *Improvement of the critical temperature of NbTiN films on III-nitride substrates*, Superconductor Science and Technology **32**, 035008 (2018).

[23] J. Rairden and C. Neugebauer, *Critical temperature of niobium and tantalum films*, Proceedings of the IEEE **52**, 1234 (1964).

[24] Z. Charifoulline, *Residual Resistivity Ratio (RRR) measurements of LHC superconducting NBTI cable strands*, IEEE Transactions on Applied Superconductivity **16**, 1188 (2006).

[25] O. Usenko, A. Vinante, G. Wijts, and T. H. Oosterkamp, *A superconducting quantum interference device based read-out of a subattonewton force sensor operating at millikelvin temperatures*, Applied Physics Letters **98** (2011).

[26] A. Kirste and J. Engert, *A SQUID-based primary noise thermometer for low-temperature metrology*, Philosophical Transactions of the Royal Society A Mathematical Physical and Engineering Sciences **374**, 20150050 (2016).

Appendix A

# Additional results

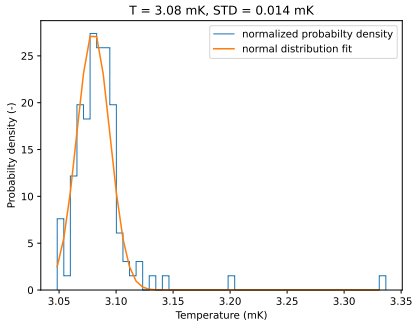


*(a) Lowest reached temperature*

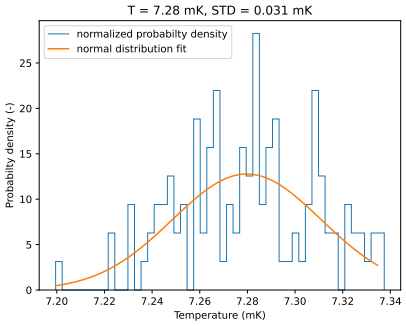


*(b) Step 1*

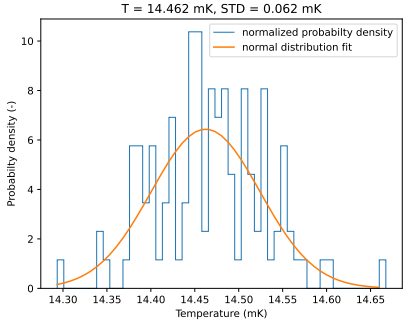


*(c) Step 2*

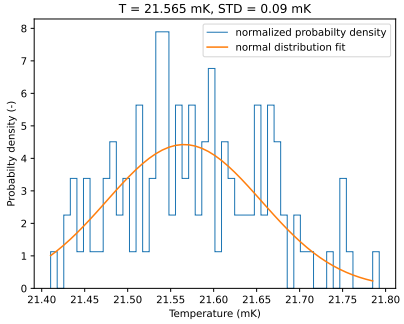


*(d) Step 3*

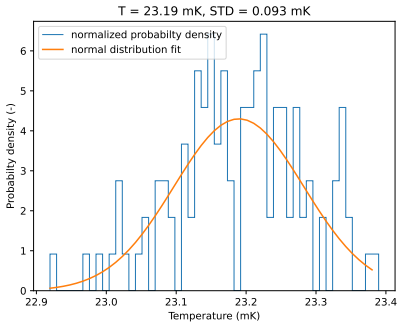


***(e)*** *Step 4*

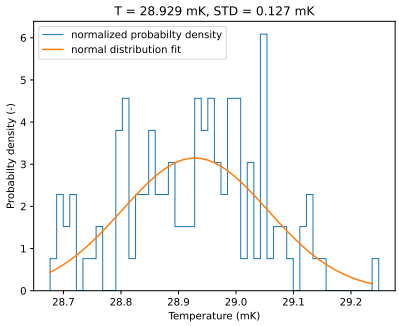


***(f)*** *Step 5*

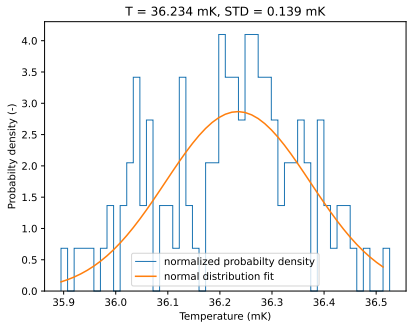


***(g)*** *Step 6*

***Figure A.1:*** *Histograms of the temperatures measured by the MFFT of each temperature step45and corresponding gaussian fit. Each histogram spans a period of two hours. All of the fits have been done using equation 4.1. The resulting average temperature and its standard deviation is given above the plot.*

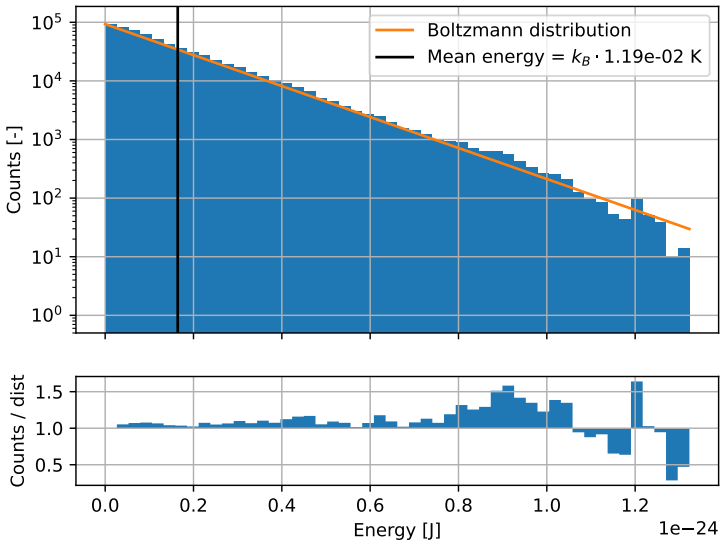


***(a)*** *Lowest reached temperature*

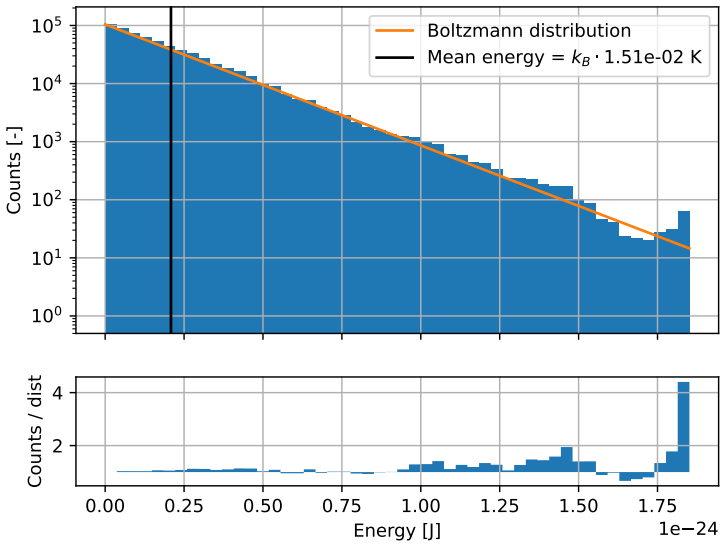


***(b)*** *Step 1*

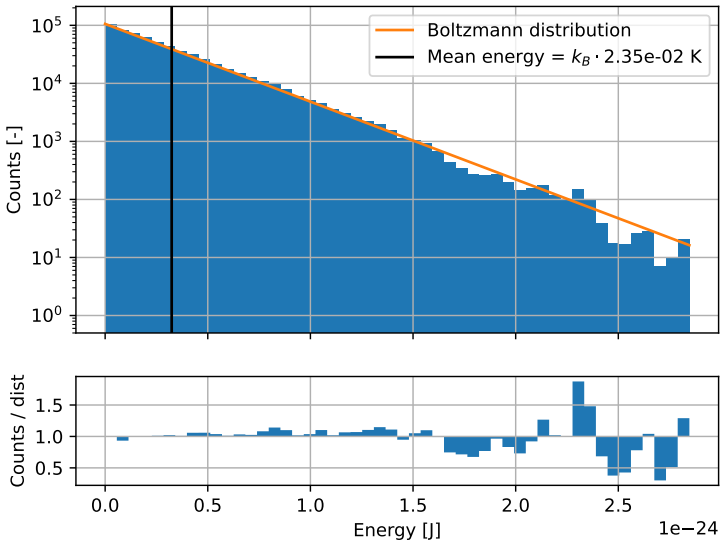


***(c)*** *Step 2*

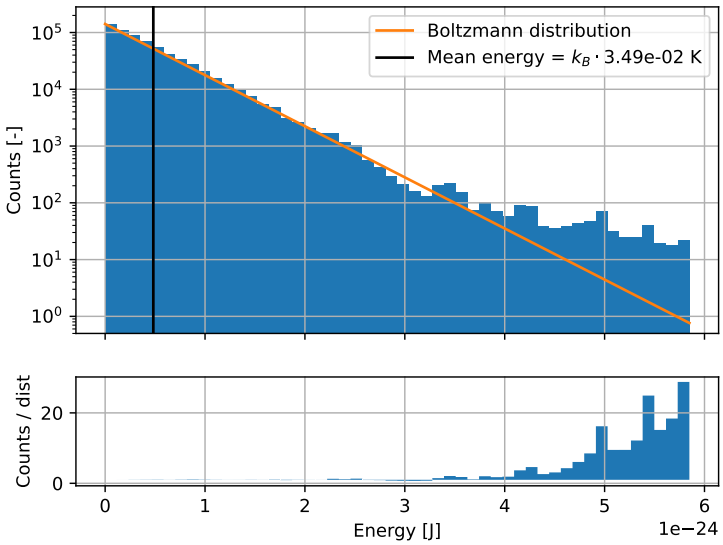


***(d)*** *Step 3*

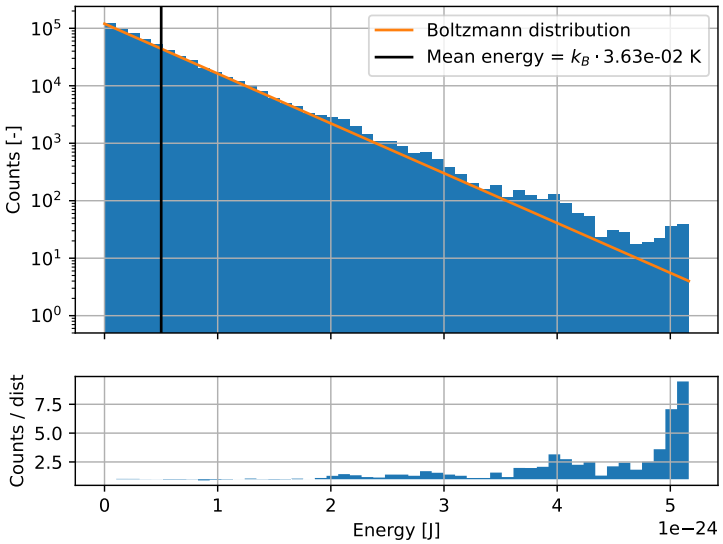


***(e)*** *Step 4*

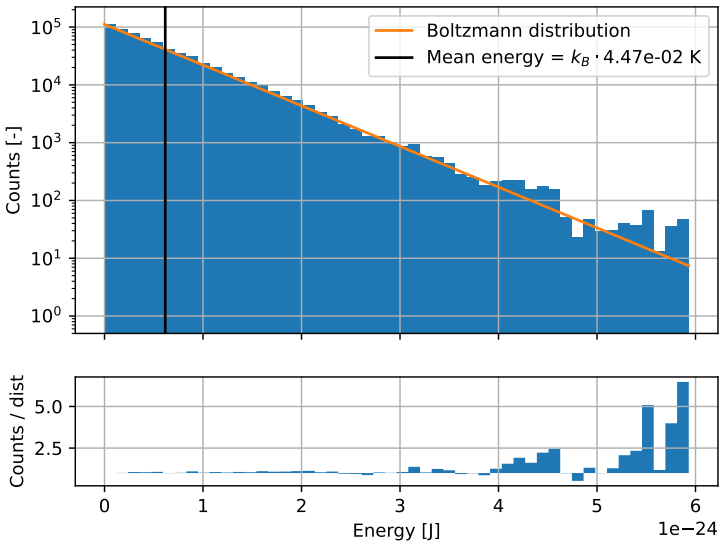


***(f)*** *Step 5*

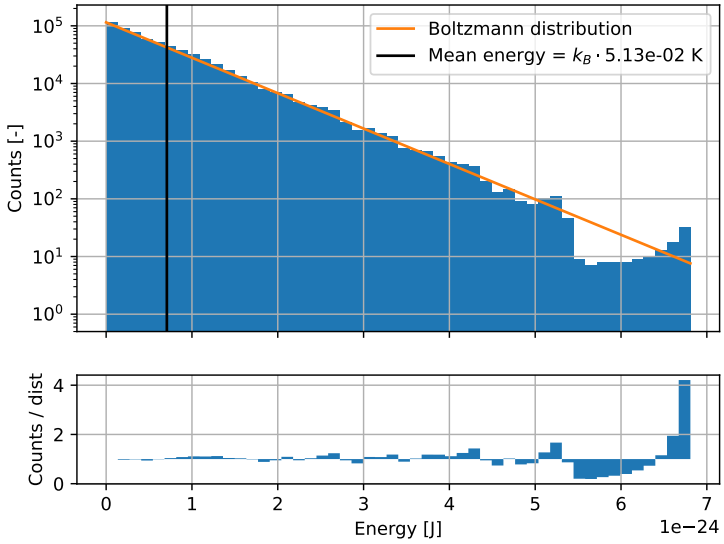


***(g)*** *Step 6*

***Figure A.2:*** *Energy histograms of the thermal motion of the cantilever during the energy steps. Each histogram describes the same two hours as the corresponding temperature histograms in figure A.1. The graph underneath the main histogram shows how much the energy distribution differs from the expected Boltzmann distribution.*